Available online at www.sciencedirect.com
ScienceDirect
Comput. Methods Appl. Mech. Engrg. 196 (2006) 634–651
Computer methods in applied mechanics and engineering
www.elsevier.com/locate/cma

Shape optimization in ship hydrodynamics using computational fluid dynamics ☆

Emilio F. Campana [a,*], Daniele Peri [a], Yusuke Tahara [b], Frederick Stern [c]

[a] INSEAN, National Ship Research Institute, Via di Vallerano 139, 00128 Rome, Italy
[b] Osaka Prefecture University, Department of Marine System Engineering, Gakuencho, Sakai 599-8531, Japan
[c] IIHR, Hydroscience & Engineering, The University of Iowa, Iowa City, IA 52242-1585, USA

Received 28 October 2005; accepted 9 June 2006

Abstract

A definite trend in computational applied mechanics is the development of integrated procedures for design optimization based on large-scale numerical simulations (Simulation-Based Design, SBD). In the present paper the fundamental elements of a SBD environment for shape optimization are presented and analyzed. The focus is on complex engineering optimization problems which involve computationally highly expensive objective functions and nonlinear constraints. Advanced strategies adopted for reducing the overall computational effort are illustrated, optimization algorithms for nonlinear programming problems are discussed as well as alternative techniques for shape variation and mesh manipulation, necessary to automatically adapt the volume grid to the evolving shapes. A new Verification and Validation (V&V) methodology for assessing errors and uncertainties in simulation based optimization is also introduced based on the trends, i.e., the differences between the numerically predicted improvement of the objective function and the actual improvement measured in a dedicated experimental campaign, including consideration of numerical and experimental uncertainties. Two different SBD versions are then presented and demonstrated on a complex industrial problem, namely the optimal shape redesign of a ship under real-world geometrical and functional constraints, whose evaluation during the optimization process involves repeated solutions of the Reynolds Averaged Navier–Stokes equations. Finally an experimental campaign is carried out on the two optimized models to validate the computations and assess the success of the optimization process. Both the optimized models demonstrate improved characteristics beyond the numerical and experimental uncertainties, confirming the validity of the SBD frameworks.
© 2006 Elsevier B.V. All rights reserved.

Keywords: Simulation based design; Shape optimization; Derivative-free optimization; Variable fidelity; Verification and validation

1. Introduction

The increasing complexity of engineering systems with the inherent difficulty to deal simultaneously with a growing number of design goals and constraints has raised the interest in the development of Simulation-Based Design (SBD) frameworks, which combine together computationally expensive analysis tools, such as Reynolds Averaged Navier–Stokes (RANS) solvers, with computer-aided design systems and efficient optimization algorithms. Modern engineering software for the design of all kind of transport systems (land, air and sea vehicles) is evolving in this direction and many authors believe that the recent advancements in the simulation of systems governed by partial differential equations (PDE) will increase the diffusion of SBD frameworks in this field, leading to innovations in shape and enhancements in performances (e.g., [4,21,22,34]).

Shape optimization has a long tradition in design engineering [30,18]. In the naval hydrodynamic context, the

☆ This work has been partially supported by the US Office of Naval Research under the grants No. 000140210489, No. N000140210304 and No. N00140210256, through Dr. Pat Purtell.
* Corresponding author. Tel.: +39 06 50299296; fax: +39 06 5070619.
E-mail address: e.campana@insean.it (E.F. Campana).

0045-7825/$ - see front matter © 2006 Elsevier B.V. All rights reserved.
doi:10.1016/j.cma.2006.06.003

rapidly growing amount of papers devoted to optimal shape design of marine vehicles (e.g., [24,39,12,37,29]) witness the increasing consideration received by shape optimization techniques in the design of efficient ships. In this framework, the redesign of the surface combatant ship DTMB 5415 (conceived by David Taylor Model Basin (USA) as a preliminary design for a US Navy surface combatant (ca. 1980) with a sonar dome bow and transom stern)[1] has been frequently used as a typical example of a highly complex shape optimization problem: Newman et al. [24] optimized the bulb using sensitivity analysis and complex variable finite-difference approach, a finite-difference gradient-based approach was followed by Tahara et al. [37] for stern and sonar dome optimization, Peri and Campana [26–29] investigated a variable-fidelity approach [2] to speed up the optimization process using free surface RANS in a multiobjective design problem.

Nonetheless, works on this topic are still subject to criticisms raised by design engineers about the excessive simplicity of the optimization problem solved when compared to the complexity of a real-life design problem. Additionally, questions are posed about final shapes obtained form the optimization process, often classified as unrealistic or too expensive to be build. Moreover, the lack of experimental evidence of the success of the optimization often shed a shadow of uncertainty on the practical usefulness of the whole procedure and on the maturity of the numerical shape optimization.

In reality, many optimization tools and SBD architectures are not sufficiently mature or appropriate for real-world applications, for a number of reasons: shape optimization of a complex geometry typically involve a large number of variables, different disciplines and conflicting objectives, requiring hundreds or thousands of function evaluations to converge to an optimal design. Furthermore, if high-fidelity CFD solvers are required as analysis tools (e.g., RANS solvers), both derivative-free and gradient-based optimization methods become more and more expensive. Another great challenge comes from the adoption of nonlinear constraints, which inevitably produce non-convex feasible design space and from multimodality of the objective functions, i.e., functions with many local minima. In such design spaces, unsophisticated use of local optimization techniques is normally inefficient for non-convexity and multimodality can easily ''trap'' local optimizers in sub-optimal designs. The use of Global Optimization (GO) algorithms can alleviate the last two problems, but, on the other end, inevitably leads to a further increase of the computational effort.

Anyhow, SBD developers have to face the challenges posed by real engineering applications, addressing problems of larger complexity and size. This is the major aim of three coordinated projects funded by the ONR and resulting in a close interaction among IIHR – Hydroscience and Engineering of the University of Iowa, the Osaka Prefecture University (OPU), and the Italian Ship Model Basin (INSEAN). The goal is to develop reliable and efficient SBD frameworks capable of dealing with complex design problems.

In the present paper, we analyze different alternatives of the SBD fundamental elements and test them in a real-life application. SBD functional components are briefly analyzed and alternatives are described: codes for CFD simulation, optimizers and geometry and mesh modification tools. Both derivative-free and derivative-based algorithms are tested as optimizers. In the former, a Genetic Algorithm approach [17,10] is adopted and modified in a ''narrow band'' approach, including the capabilities of high performance computing, with a portable, multilevel parallelism for dynamic load balance. In the second SBD framework, since the multigrid technique used in the RANS solver naturally provide a set of meshes of various refinement, a particular variable-fidelity model (AMMO, Approximation Model Management Optimization, [1–3]) has been used to reduce the computational effort in the computation of the gradient of the objective function.

The two SBDs are also based on different high-fidelity RANS solvers adopted for the analysis. At the Gothenburg international CFD workshop the DTMB 5415 was selected as a benchmark representative of navy designs and used to test up-to-date free surface RANS solvers. The two analysis tools adopted in this paper, namely CFDSHIP-Iowa [25] and MGShip [11], classified in the workshop as the best two codes on this test case, demonstrating the accuracy of their prediction [19]. Different techniques for shape and grid manipulation (CAD-free and CAD-based) have been also adopted during the optimization process.

With the aim of exploring the effectiveness of alternative strategies, two SBD environments are eventually developed with different components and used to solve a single objective function problem relative to the navy ship DTMB 5415. In the problem, complexity has been introduced by (i) enforcing nonlinear, real-life geometrical and functional constraints, to provide realistic final optimal designs, (ii) adopting accurate (but CPU-time expensive!) PDE solvers in the analysis of the sub-optimal configurations and (iii) demonstrating the success of the optimization by carrying out a dedicated experimental campaign to assess the real enhancements in the explored objective function.

The region of the ship subject to change is restricted to the bow and the sonar dome (about 20% of the overall ship surface). The nature of the problem is hence the redesign of some part of an already existing complex system, a quite difficult test which only allow a very reduced freedom to the optimizer and explains the use of local optimizers. Furthermore, realistic constraints have been enforced in the problem. Adopted functional constraints are connected with the ship's operability and propulsion. Geometrical constraints enforced refer to the displacement, the major ship's dimensions, the bow entry angle, and the sonar dome

[1] The geometry of the DTMB 5415 can be downloaded from the web site: http://www.iihr.uiowa.edu.

position and minimum width. In this paper the problem is formulated for the bare hull, hence partially reducing some of the geometrical complexities (e.g., no appendages and propellers will be considered here) which however are ineffective in the redesign of the bow.

Finally, to assess the success of the optimization process, a dedicated experimental campaign on the original and on the optimized models has been carried out. The experimental data are then used in a new verification and validation (V&V) procedure based on the analysis of the trend of the objective function to be minimized. This procedure represents an extension of the one proposed by Stern et al. [33,41] for single numerical simulations and piggyback on Coleman and Stern [9] validation approach for trends by adding the verification considerations. Indeed, due to the inherent uncertainties in simulations and experiments the success of an optimization process is more appropriately based on trends than absolute values. Reported results demonstrate the success of both the SBD environment developed. The extension of the developed SBDs to multi-objective, global optimization is the authors' current effort [6,38] and will be presented in a sequel paper.

2. Basic elements of simulation-based design optimization

Shape design optimization is typically formulated in the framework of Nonlinear Programming (NLP) problem. The mathematical formulation assembles all the design variables $x_1, x_2, \ldots, x_N$ in a vector $\boldsymbol{x} = (x_1, x_2, \ldots, x_N)^{\mathrm{T}}$ belonging to a subset χ of the N-dimensional real space $\Re^N$, that is $x \in \chi \subseteq \Re^N$ (upper x_i^{u} and lower x_i^{l} bounds are typical enforced onto the design variables). The objective of the optimization f and the equality and inequality constraints h, g are functions of the design variables $\boldsymbol{x}$ and of the state of the system $\boldsymbol{u}$. A general form for constrained NLPs is then to find the particular vector $\tilde{x}$ in the subset χ which solves the following:

$$\begin{aligned} \min \quad & f(\boldsymbol{x}, \boldsymbol{u}(\boldsymbol{x})) \quad x = (x_1, x_2, \ldots, x_N)^{\mathrm{T}}, \\ & x \in \chi \subseteq \Re^N \\ \text{subject to} \quad & h_j(x) = 0, \quad j = 1, \ldots, M, \\ & g_j(x) \leqslant 0, \\ & x_i^{\mathrm{l}} \leqslant x \leqslant x_i^{\mathrm{u}}, \quad i = 1, \ldots, N. \end{aligned} \tag{1}$$

The physical state of the system is numerically evaluated by solving a system of PDE of the general form $A(\boldsymbol{x}, \boldsymbol{u}(\boldsymbol{x})) = 0$.

The solution of this problem typically requires the use of some numerical tool – the first fundamental element of the SBD framework, Fig. 1 – to solve the system $A(\boldsymbol{x}, \boldsymbol{u}(\boldsymbol{x}))$ and evaluate the current design $\boldsymbol{x}$, obtaining information on the constraints too. If the function used to define the optimization problem is of fluid dynamic nature, as in our case, the step requires the evaluation of the design $\boldsymbol{x}$ via a CFD solver, a process which is itself computationally intensive. Within a standard nonlinear optimization algorithm (Fig. 1) the solution of these differential equations is required

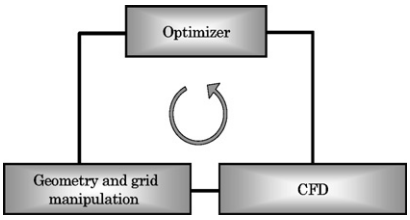

Fig. 1. Basic elements of a CFD-based optimization environment.

for *each* iteration of the algorithm. In addition to these two elements, a third one is necessary: a geometry modeling method to provide a link between the design variables and a body shape. When the analysis tools is based on the solution of a PDE on some volume grid around a complex geometry this task is not a trivial one and often requires some attention. The flexibility of this element may greatly affect the freedom of the optimizer to explore the design space.

In the following, two different approaches are investigated for each component.

2.1. Optimizer

In the detailed design phase of complicated systems like ships, the use of low-fidelity analysis tools does not guarantee real improvements, especially when the margin for improvement is small. Complex, high-fidelity CFD solvers such as free surface RANS codes might then become necessary.

A major problem to face with is then that one can be overcome by the model's computational expense. Indeed, the use of these expensive analysis tools in iterative procedures introduces *per se* a relevant problem to solve, both in derivative-free and derivative-based approaches. Hence, in the following we will indicate for both these approaches two alternative ways to reduce the overall computational effort.

2.1.1. Narrow band derivative-free approach

Genetic Algorithms (GA) are a stochastic search technique that perform a multiple directional search by maintaining a population of potential solutions. In the present case a so-called "Narrow Band" approach is used, meaning with this that the population used is small and that the bounds for the variables are narrow, so that the search remains confined in a relatively small design space, mimicking a derivative-free local optimization technique.

The adopted algorithm proceeds as follows: (i) generation of an initial population of individuals at random manner; (ii) decoding and evaluation of some predefined quality criterion, referred to as the fitness; (iii) selection of individuals based on a probability proportional to their relative fitness; (iv) crossover and mutation. The steps (ii) through (iv) are repeated until the generation achieves designated number. The objective function F_{obj} is related to the fitness function f_o, a form of Sigmoid function in the present study, i.e.,

$$\text{For maximization:} \quad f_o = \frac{1}{1+\mathrm{e}^{-F_{\text{obj}}}},$$

$$\text{For minimization:} \quad f_o = \frac{1}{1+\mathrm{e}^{F_{\text{obj}}}}$$

and constraints are accounted for by using a penalty function approach, which yields resultant fitness f given by

$$f = f_o + r\left[\sum_{j=1}^{M}|h_j(x)| + \sum_{j=1}^{N}|\min\{0, -g_j(x)\}|\right],$$

where r is penalty parameter. GA is generally capable for finding global minimum/maximum within the design space. In a form of mathematical model, the genotype is represented as frequency. For instance, the frequency of genotype B_i at generation $t+1$, i.e., $x_i(t+1)$ is given in terms of frequency at generation t as follows:

$$\text{Selection:} \quad x_i(t+1) = \frac{f_i}{\bar{f}(t)}x_i(t) \quad (i = 1, \ldots, n),$$

where n is population size, f_i is a fitness of B_i, and $\bar{f}(t)$ is the average fitness of a population. In similar manner, change in the frequency through crossover and mutation are given by

$$\text{Crossover:} \quad x_k(t+1) = \sum_{i=1}^{n}\sum_{j=1}^{n} C(k|i,j)x_i(t)x_j(t),$$

$$\text{Mutation:} \quad x_i(t+1) = \sum_{j=1}^{n} M_{ij}x_j(t),$$

where C is a crossover tensor, and M_{ij} is a mutation matrix which stands for the probability of mutation from B_j to B_i over one generation. C and M includes crossover and mutation ratios, both of which are system parameters. Evaluation of effectiveness of GA is often discussed [17], but that will not be the main objective of the present paper. It is known that Simulated Annealing (SA), a related global optimization technique, can also be used within a standard GA algorithm, simply by starting with a relatively high rate of mutation, which decreases over time along a given schedule.

As stated before, in the present study the design space is relatively narrow banded; therefore, other advantages of GA are here more highlighted, namely the derivative-free nature and high adaptableness for parallel computing, i.e., intrinsic parallelism. Indeed, the conventional GA algorithm has been adapted for parallel computing by using the Message Passing Interface (MPI) protocol [36]. Fig. 2 shows the difference between the present parallel GA architecture and the conventional serial computations. For the former case, processor 0 controls overall GA procedure, and processors 1 through m, where m is number of population, simultaneously execute CFD method, i.e., evaluation of $f(\vec{\beta}_i)$ in the figure. The parallel architecture offers advantage over the serial architecture for considerably higher computational efficiency, i.e., computational speed of the former is nearly m times faster than that of the latter, since most of CPU time is used for CFD method, and communication overhead is basically small. Furthermore, computational speed for GA in parallel architecture does not depend on number of population as well as number of design parameters.

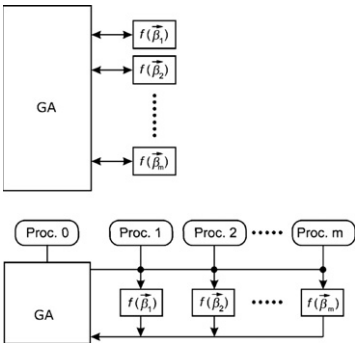

Fig. 2. Serial and parallel architecture of the Narrow Band-GA optimizer.

2.1.2. Derivative-based variable-fidelity approach

When expensive computer codes (those necessary to solve complex *high-fidelity* models) are used into the solution of the optimization problem, the overall computational time might become unaffordable and the introduction of cheaper approximations (*low-fidelity* models) is unavoidable. The idea of using low-fidelity, inexpensive models, together with occasional (heuristic) recourse to high-fidelity, more expensive models (for monitoring the progress of the algorithm) has been used in engineering for long time. Several versions may be implemented, depending on the type of the variable-fidelity model: variable grid density, variable iterative accuracy, variable physics.

A *systematic* approach (in contrast to heuristic approaches) is explored in the present paper, the *variable-fidelity/first-order trust region* AMMO method proposed by Alexandrov and Lewis [1–3]. The ability of the low-fidelity model to guide the optimization process is monitored and its quality may be improved when required, while consistency constraints are enforced to ensure global convergence to the original high-fidelity solution.

This AMMO variable-fidelity framework can be used with any derivative-based method and set of models, including cases where gradients are computed via adjoints or via automatic differentiation [5,13,15]. In our case, we are focusing on zero-order methods, because the problems in question have a sufficiently small number of variables, and because zero-order methods may have additional smoothing effects that assist in not being stuck in local optima.

Let us suppose to have two models for computing our objective function f and that they can both be used as analysis tool: a simple low-fidelity model (f_l), computationally cheap, and a high-fidelity model (f_i) more accurate but also more expensive. We can define their ratio as a scale factor $\beta(x)$, function of the design x, the vector which contains all the design variables:

$\beta(x) = f_h(x)/f_l(x)$.

We can use this scale factor to improve the quality of the lower approximation model. To this aim we need a model for $\beta(x)$ and this can be easily build by a first-order local approximation $\beta_{loc}(x)$ of $\beta(x)$ around the current design $\boldsymbol{x}^k$:

$$\beta_{loc}(x) = \beta(x^k) + \nabla\beta(x^k)^T(x - x^k).$$

This local approximation is then used to correct (to the first-order) the value obtained with the low-fidelity model f_l:

$$f_h(x) = \beta(x)f_l(x) \approx a(x) = \beta_{loc}(x)f_l(x),$$

where $a(x)$ is now the improved approximation which satisfies the following consistency conditions:

$$a(x^k) = f_h(x^k),$$
$$\nabla a(x^k) = \nabla f_h(x^k).$$

Being based on quantities local to $\boldsymbol{x}^k$ however, one has to keep in mind that the approximation $a(x)$ cannot be applied in the whole design space and that, since we are progressively moving away from $\boldsymbol{x}^k$. The validity of the approximation must be monitored in some way: the trust-region method offer a systematic way to perform this monitoring and is therefore adopted here in order to determine the region (of radius r) in which we can still *trust* the correction factor $\beta_{loc}(x)$ build at the design $\boldsymbol{x}^k$.

At the k-step a general algorithm has the following general form:

1. Compute the gradient of the corrected low-fidelity model $\nabla a(x^k)$;
2. Using a and $\nabla a(x^k)$ solve the optimization problem and obtain the descent step s^k under the constraint $\|s^k\| \leqslant r$;
3. The new design is given by the vector $\boldsymbol{x}^{k+1} = \boldsymbol{x}^k + s^k$;
4. Measure the progress made: compute the ratio between the real and the expected improvement at the new design $\boldsymbol{x}^{k+1}$:

$$R = \frac{f_h(x^k) - f_h(x^{k+1})}{f_h(x^k) - a(x^{k+1})}.$$

5. Analyze R:
   - a value close to 1 means that the model $a(x)$ predicts the real behavior exceptionally well and that the trust region radius r might be increased;
   - a value far from 1 means that the correction factor $\beta_{loc}(x)$ is no more reliable and causes the step to be rejected. Reduce the trust region radius r. Should the radius become too small $\beta_{loc}(x)$ and $a(x)$ must be recomputed;
   - the step is accepted otherwise, without altering the r value.

It must be underlined that the estimation of the gradient with the expensive f_i model is only required when the correction $a(x)$ has to be newly computed, since $\nabla a(x^k)$ is needed. The formulation adopted for the correlation law (the scale factor $\beta(\boldsymbol{x})$) is due to Haftka [16] and [7].

Flexibility, effectiveness and easiness of implementation are strong points of this algorithm. Finally, we stress that the final optimized shape obtained is the same as if a high-fidelity model was used during all the process. Indeed, the consistency condition derived before ensure the quality of the "corrected" lower fidelity model, telling us when the local approximation cannot be trusted anymore and has to be re-build.

2.2. Geometry and grid manipulation

Tools for geometry modeling (and its necessary sequel, the automatic grid deformation) are another relevant SBD component. An efficient and flexible way to modify the geometry of the body is necessary for a full investigation of the design variables space and a successful optimization. Techniques should be enough versatile to describe a broad variety of complex 3D configurations and sufficiently compact so to use as few variables as possible. Once the optimization algorithm obtains the vector with the new design variable values, we have to spread the deformation over the body surface and the computational volume grid. Flexible methods are the superposition of several basic forms (morphing techniques) or the expansion/reduction of basic geometry. Another capable method for geometry modeling is through application of CAD systems. In the present study, two approaches are investigated: i.e., a CAD-based approach and an additive perturbation (CAD-free) method.

2.2.1. CAD based

Both based on a CAD system, two approaches are possible, i.e., CAD direct control and CAD emulation approaches. The implementations into optimization environments are shown in Figs. 3 and 4. In the former, optimizer directly executes CAD macro file in which procedures are pre-described for hull form modification and evaluation of constraint function. In the latter, a module is implemented in order to emulate CAD operation handling with the mathematical surface modeling. For example, the Non-Uniform Rational B-Spline (NURBS) is widely used in CAD system for hull-form design as IGES entity 128. NURBS surface is mathematically given by

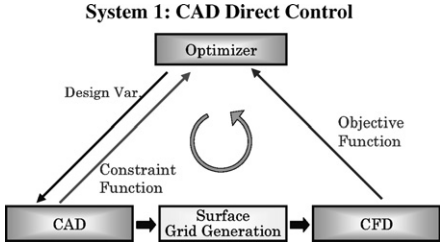

Fig. 3. Implementation of the CAD-based hull form modification into optimization environment: System 1 (CAD direct control).

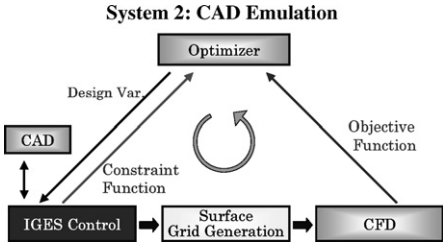

Fig. 4. Implementation of the CAD-based hull form modification into optimization environment: System 2 (CAD emulation).

$$\mathbf{S}(u,v)=\frac{\sum_{i=0}^{n}\sum_{j=0}^{m}N_{i,p}(u)N_{j,q}(v)w_{i,j}\mathbf{P}_{i,j}}{\sum_{i=0}^{n}\sum_{j=0}^{m}N_{i,p}(u)N_{j,q}(v)w_{i,j}},$$

where, u and v are parameters, $N_{i,p}$ and $N_{i,q}$ are normalized B-spline basis functions of degree p and q in u and v directions, respectively, $P_{i,j}$ are location vectors of control points, and $w_{i,j}$ are weights. Finally, the surface is defined by $(n+1)*(m+1)$ control points, weights and not vectors U and V of $n+p+2$ and $m+q+2$ elements in u and v directions, respectively.

The CAD emulation approach offers an advantage over the former for complete independence from CAD system, i.e., designers are able to use any CAD system and give/receive initial/optimized hull form geometry in IGES format data. A modified surface is defined in correspondence to new location vectors $\mathbf{P}^{\mathrm{n}}$, so that

$$\mathbf{P}^{\mathrm{n}}_{i,j}=\mathbf{P}^{\mathrm{o}}_{i,j}+\delta\mathbf{P}_{i,j},$$

where $\mathbf{P}^{\mathrm{o}}$ and $\delta\mathbf{P}$ are original and displacement location vectors. $\delta\mathbf{P}$ can be design variables of the optimization problem.

2.2.2. Additive perturbation (CAD-free) method

With this approach, the use of CAD is avoided and the deformation of the shape is defined and controlled by using a few control points, much less than the number of nodes used for the discretization adopted for the flow analysis. The method is based on the use of Bezier polynomial patches. The underlying idea is not to model the body's shape with Bezier surfaces (this will leads to inevitable problems when dealing with non-smooth objects) but just the deformation $\boldsymbol{d}^k$ from the original shape $\boldsymbol{x}^0$. The polynomial curve

$$B_n(t)=\sum_{i=0}^{n}\binom{n}{i}(1-t)^{n-i}t^i p_i$$

is a Bezier curve of degree n. A Bezier patch is the surface extension of the Bezier curve. At the step k the new design x^{k+1} is given by

$$x^{k+1}=x^k+s^k=x^0+d^k=x^0+\sum_{i=0}^{1}\sum_{j=0}^{m}\sum_{k=0}^{n}B_i^l B_j^m B_k^n.$$

The geometry is simply modified by superimposing one or several Bezier surfaces to the original ship's geometry, each one accounting for the deformation relative to some part of the body. Each Bezier patch is controlled by a given number of control points $\boldsymbol{p}$ that are used as design variables by the optimizer. Number and position of the patches and number of control points per patch can be changed in an easy and flexible way, depending onto the details of the assigned problem. At the junction between two patches continuity on the first and second derivative can be enforced to ensure the fairing of the body's surface. Applications of this method can be found in Peri and Campana [27].

2.2.3. Grid manipulation

Once the ship surface is modified, the volume grid around the hull should change accordingly with a simple adaptive algorithm. The same grid manipulation is used in association with both methods.

During the optimization, the grid is updated at every optimization cycle as the hull form is modified. This is accomplished by the use of an algebraic scheme to increase the computational efficiency. A similar approach was used by Tahara et al. [37] and Peri and Campana [27]; however, more simplified scheme was found effective in the present study. The method is described in the following. After an initial grid is generated, the geometrical information is computed and stored in the memory, that is as follows:

$$\begin{cases}P=S^1(\xi^1,\xi^2,\xi^3),\\ Q=S^2(\xi^1,\xi^2,\xi^3),\\ R=S^3(\xi^1,\xi^2,\xi^3),\end{cases}$$

where P,Q,R are grid clustering and stretching functions defined in the (ξ^1,ξ^2,ξ^3) directions, respectively. More specifically, those are normalized metric of (ξ^1,ξ^2,ξ^3) coordinates, such that $0\leqslant S^i\leqslant 1$, and $S^i=0$ and $S^i=1$ for $\xi^i=1$ and $\xi^i=\xi^i_{\max}$, respectively. The grid points for the original geometry are already defined in computational coordinates, i.e.,

$$\begin{cases}x=x_0(\xi^1,\xi^2,\xi^3),\\ y=y_0(\xi^1,\xi^2,\xi^3),\\ z=z_0(\xi^1,\xi^2,\xi^3)\end{cases}$$

and the hull surface is expressed as

$$\begin{cases}x=x_0(\xi^1,1,\xi^3),\\ y=y_0(\xi^1,1,\xi^3),\\ z=z_0(\xi^1,1,\xi^3),\end{cases}\quad\text{and}\quad\begin{cases}x=x_m(\xi^1,1,\xi^3),\\ y=y_m(\xi^1,1,\xi^3),\\ z=z_m(\xi^1,1,\xi^3),\end{cases}$$

where ξ^2 is taken to be normal direction to the surface, and values with subscript 0 and m correspond to the original and modified hull surfaces. The grid points at the outer boundary is fixed and given by

$$\begin{cases}x=x_0(\xi^1,\xi^2_{\max},\xi^3),\\ y=y_0(\xi^1,\xi^2_{\max},\xi^3),\\ z=z_0(\xi^1,\xi^2_{\max},\xi^3).\end{cases}$$

In the optimization procedure, the hull surface is modified but other computational boundaries. In the work of Tahara [37], all grid points are relocated using P, Q, and R when the surface is modified, and an iterative manner is used to complete the procedure. On the other hand, simpler grid relocation method can be applied if the modification is assumed to occur in local scale. That is, the method is based on only Q and simply written as

$$\begin{cases} x = x_0(\xi^1,\xi^2,\xi^3) + (x_m(\xi^1,1,\xi^3) \\ \quad -x_0(\xi^1,1,\xi^3))(1-S^2(\xi^1,\xi^2,\xi^3)), \\ y = y_0(\xi^1,\xi^2,\xi^3) + (y_m(\xi^1,1,\xi^3) \\ \quad -y_0(\xi^1,1,\xi^3))(1-S^2(\xi^1,\xi^2,\xi^3)), \\ z = z_0(\xi^1,\xi^2,\xi^3) + (z_m(\xi^1,1,\xi^3) \\ \quad -z_0(\xi^1,1,\xi^3))(1-S^2(\xi^1,\xi^2,\xi^3)). \end{cases}$$

Although the method is relatively simple and straightforward, it was found able to keep the grid quality nearly equal to the original one.

2.3. Simulation tool

For an advanced fluid dynamic redesign of an existing vehicle on the base of its drag, accurate fluid dynamics analysis tools are necessary for guiding the optimizer toward improved solutions. In the present study, both for the evaluation of the objective function R_t and of the functional constraint on the sonar dome vortices, the use of free-surface RANS equation solver, whose degree of reliability has constantly matured during the last years, is necessary. The corresponding equations are outlined, for instance, in Tahara and Stern [35]. Two fundamental parameters (neglecting surface tension effects) come to play in these simulations: the Froude number $Fr = U/(gL)^{1/2}$ and the Reynolds number $Re = UL\rho/\mu$, being U and L the speed and the overall length of the ship, respectively.

The Gothenburg 2000 [14] international workshop on the numerical prediction of the turbulent flow around ships was focused on testing three modern hull forms, among which the DTMB 5415 was selected to represent navy designs. Verification and validation procedures were performed and the workshop showed that total resistance, wakes and free-surface waves might now be well predicted by some of the best codes. CFDSHIP-Iowa [40] and MGShip [11], the two analysis tools adopted in this paper, were identified as the best two codes on the DTMB 5415 tests case, as reported by Larsson et al. [19].

CFDSHIP-Iowa is a general-purpose, multiblock, MPI-based high-performance, unsteady RANS CFD code [40,42] developed for computational ship hydrodynamics which solves the three-dimensional unsteady incompressible RANS equations. In the version adopted for the present paper, the grid dynamically conforms to the solution of the exact kinematic free-surface boundary condition. Approximate dynamic free-surface boundary conditions provide boundary conditions for velocity and pressure. Reynolds-stress closure is accomplished through k–omega turbulence model. The solution scheme is based upon the PISO algorithm and is fully implicit. The convective and viscous terms are discretized with second-order upwind and second-order central differences, respectively. The pressure equation is obtained by taking the divergence of the momentum equations. Further description and related references can be found at http://www.iihr.uiowa.edu/cfdship.

MGShip [11] is a multigrid (FAS-FMG), multiblock, structured grid code, which uses a surface fitting approach to compute the wave pattern. The mathematical model is based on a pseudo-compressible formulation of the RANS equations, approximated in the discrete formulation by a finite volume technique. A second-order ENO-type scheme is adopted for non-viscous terms, while viscous fluxes are computed by a standard centered finite volume approximation. Reynolds-stress closure is accomplished through Spalart and Allmaras [31] turbulence model. MGShip has been extensively validated and is currently used by the It. Navy, as well as ship (aeronautical) industries for hydro- (aero-) dynamic simulations. More information on MGShip may be found in proceedings of Gothenburg workshops.

For the evaluation of the seakeeping characteristics of the hulls, the adopted simulation tool (Ship Motion Program (SMP) [20]) is based on a strip theory approach (for an outline of the approach see, for instance, Newman, 1977 [23]) and on a potential flow model. The SMP computes the motions for the ship advancing in arbitrary headings in regular and irregular seas. Due to the use of potential flow model SMP is more accurate for computing vertical motions (as heave and pitch motions) than for the roll motion, typically affected by the shedding of vorticity from the bilge keels. For this reason it has been used in the present paper to evaluate the constraint of the seakeeping (Table 1) which is formulated in terms of the peak of the Response Amplitude Operator (RAO) curve. For a particular ship response the RAO is the square of the amplitude of the regular wave transfer function at each frequency.

2.4. Integration of optimization components and simulation based design environment

All the above-mentioned optimization components are integrated to yield two optimization approaches, i.e., SBD-A and SBD-B. Optimizations using those environments are demonstrated at OPU and INSEAN, respectively. In the following, those approaches are summarized in association with additional information regarding the simulation based design environment.

SBD Version A: The Narrow-Band Derivative-Free Approach, the CAD-Based and grid manipulation method, and the CFD-SHIP Iowa RANS solver version 3.02 compose the SBD-A. For the present application, the System-2 (CAD Emulation) is selected for the geometry method. The integrated system also involves the SMP code to evaluate the RAO, which are part of constraints described

Table 1
The definition of the nonlinear constrained optimization problem

Type	Definition	Note
Objective function	$\min R_T(Fr, Re)\ x \in \Re^{N_{dv}}$	Bare hull, fixed model, $Fr = 0.28$, $Re = 1.67 \times 10^7$
Functional constraints		
On seakeeping	$S_C = 0.5\frac{\xi_3^0}{\xi_3^p} + 0.5\frac{\xi_5^0}{\xi_5^p} \leqslant 1$ $H_C = \frac{\xi_3^0}{\xi_3^p} \leqslant 1.02$ $P_C = \frac{\xi_5^0}{\xi_5^p} \leqslant 1.02$	ξ_3, peak heave RAO ξ_5, peak pitch RAO o, optimized; p, parent All the quantities computed for $\lambda^* \geqslant 0.4$
On sonar dome vortices	$\sqrt{\frac{1}{N}\sum_i^N (\omega_x^0)_i^2} / \sqrt{\frac{1}{N}\sum_i^N (\omega_x^p)_i^2} \leqslant 1,\ \forall i \in R_C$	R_C is a circular region placed at $x = -0.30$, centered at $y = 0.02$, $z = -0.07$, with radius $r = 0.018$. o, optimized; p, parent
Geometrical constraints		
Bow entry angle	Maximum amplitude variation of 5°	2.5° per side
Sonar dome dimension	A sonar array of radius R_s and height H_s should fit inside the dome	$H_s = 3$ m, $R_s = 2.5$ m in ship length
Sonar dome position	Maximum forward position fixed	
Main dimensions	Lpp and depth fixed	
Displacement	Maximum variation ±2%	

later. The computations are performed on 64 CPU PC Cluster (Intel Xeon 2.4 GHz × 64; see [36]) which is recently designed by the authors for the present research project.

SBD Version B: In the present version of the SBD-B, the optimizer adopts the variable fidelity approach in the "*variable-grid*" formulation. Indeed, being the RANS solver MGShip based on a multigrid technique, we already have a suite of meshes that could be used to this aim. The finest and the second finest grid have been assumed as the high- and the low-fidelity models. The Derivative-Based Variable-Fidelity Approach, the Additive Perturbation Method with the grid manipulation described before, and the MGShip RANS solver, composes the SBD-B. As for the SBD-A, the SMP code is used to evaluate the heave and pitch RAOs. The computations are performed on a Pentium IV (1.7 GHz).

3. Verification and validation approach for SBD

The growing need and importance of CFD accuracy estimation pushes toward the adoption of quantitative assessment of numerical and modeling simulation errors and uncertainties. These information can be gathered through a V&V study, a procedure that needs numerical uncertainty analysis (iterative and grid convergence studies) and benchmark experimental data and uncertainty analysis and can be conducted for both integral quantities and local flow variables. For complex geometries, such as those arising in practical applications, these procedures may imply a considerable computational effort, since the necessary simulations are required to be as close as possible to the asymptotic range for the study to be accurate. This difficulty is partially responsible for the slow diffusion of these procedures, but the need for a quantification of the errors in the prediction is increasing by the hour, and eventually the CFD community will be forced to complete the predictions with an estimation of the numerical uncertainties.

The scenario changes substantially when simulations are used in a design cycle to "guide" an optimizer through the design space in the quest for an optimum. In this case, the successful application of the V&V approach to single simulations might well certify the accuracy of the numerical tool adopted in the optimization process but, on the other end, it does not imply the success of the optimization. In other words, the certification of an *isolated* numerical solution is ineffective from a designer standpoint, and the fundamental issue is the development of a procedure to validate the optimizer as a whole, involving performance's *trends* rather than their absolute values: indeed, the ultimate goal of the designer is the identification of a new shape showing improved performances with respect to an original design.

Validation of trends was discussed by Coleman and Stern [9] wherein it is noted that the inclusion of the correlated bias errors in the estimate of the experimental uncertainty offers the chance for a significant reduction in the experimental uncertainty, allowing for a more stringent validation criterion based on the difference more than on the absolute magnitudes of the variables. In the following, Coleman and Stern [9] validation approach for trends is extended to include detailed considerations on verification procedures, as done by Stern et al. [33,41] for simulations, i.e., absolute values.

A two stages V&V procedure is here adopted. The first phase concerns the estimate of simulation uncertainty relative to the initial and final designs separately and the methodology is briefly summarized here for completeness. The procedure can be applied to any simulated variable, both local and global. In a second stage, the standard V&V approach is modified to deal with the optimization process, focused on the trend of the objective function to be minimized.

3.1. V&V approach for single numerical simulations

The simulation error δ_S is defined as the difference between a simulation result $\mathscr{S}$ and the truth $\mathscr{T}$ and is composed of simulation modeling δ_{SM} and numerical δ_{SN} errors. The equation error is

$$\delta_S = \mathscr{S} - \mathscr{T} = \delta_{SN} + \delta_{SM}. \tag{2}$$

The simulation modeling error δ_{SM} is defined as the difference between the model $\mathscr{M}$ and the true $\mathscr{T}$ values, while the simulation numerical error δ_{SN} is defined as the difference between the simulation $\mathscr{S}$ and the model $\mathscr{M}$ values

$$\delta_{SM} = \mathscr{M} - \mathscr{T}, \quad \delta_{SN} = \mathscr{S} - \mathscr{M}, \tag{3}$$

where $\mathscr{M}$ is obtained by an exact solution of the continuous equations used to model the truth $\mathscr{T}$. The uncertainty equation corresponding to the error Eq. (2) is

$$U_S^2 = U_{SN}^2 + U_{SM}^2. \tag{4}$$

The *Verification* procedure is dedicated to the assessment of the simulation numerical uncertainty U_{SN} and, under some assumptions, to the estimation of δ_{SN}. The latter is typically decomposed into contributions from iteration number δ_I, grid size δ_G, time step δ_T, and other parameters δ_P, and an analogous decomposition can be applied to simulation numerical uncertainty U_{SN}^2, giving

$$U_{SN}^2 = U_I^2 + U_G^2 + U_T^2 + U_P^2. \tag{5}$$

In the present case δ_P is neglected and, since only steady-state simulations are performed, δ_T is assumed to be zero: hence, the previous uncertainty equation simplify into

$$U_{SN}^2 = U_I^2 + U_G^2. \tag{6}$$

Validation is the complementary part of verification, i.e., the process of assessing the simulation modeling uncertainty U_{SM} by using benchmark experimental data. Analogously to what done for the simulation error, we may introduce δ_D as the error on the data defined as the difference between a measurement $\mathscr{D}$ and the truth $\mathscr{T}$ ($\delta_D = \mathscr{D} - T$) which in turn leads to

$$\mathscr{D} - \delta_D = \mathscr{S} - \delta_S. \tag{7}$$

The comparison error $\mathscr{E}$ is then given by the difference between the data $\mathscr{D}$ and the simulation $\mathscr{S}$:

$$\mathscr{E} = \mathscr{D} - \mathscr{S} = \delta_D - \delta_S = \delta_D - (\delta_{SMA} + \delta_{SPD} + \delta_{SN}), \tag{8}$$

where error simulation modeling error δ_{SM} has been decomposed into the sum of δ_{SPD}, error from the use of previous data (such as fluid properties) and δ_{SMA}, error from modeling assumptions

$$\delta_{SM} = \delta_{SMA} + \delta_{SPD}. \tag{9}$$

The corresponding uncertainty equation is

$$\begin{aligned} U_{\mathscr{E}}^2 &= U_{\mathscr{D}}^2 + U_{SM}^2 + U_{SN}^2 \\ &= U_{\mathscr{D}}^2 + U_{SMA}^2 + U_{SPD}^2 + U_{SN}^2. \end{aligned} \tag{10}$$

To determine if validation has been achieved, $\mathscr{E}$ must be compared to the validation uncertainty U_V, defined as the combination of all the uncertainties contained in U_E^2 that we know how to estimate, i.e., all the uncertainties but U_{SMA}^2

$$U_V^2 = U_{\mathscr{E}}^2 - U_{SMA}^2 = U_{\mathscr{D}}^2 + U_{SPD}^2 + U_{SN}^2. \tag{11}$$

Finally, if

$$|\mathscr{E}| \leqslant U_V, \tag{12}$$

the combination of all the errors in $\mathscr{D}$ and $\mathscr{S}$ is smaller than or equal to U_V and validation is achieved at the U_V interval.

3.2. V&V approach for CFD-based optimization

The V&V procedure illustrated before can be used to estimate the accuracy of the numerical tools adopted but it cannot be of any help in assessing the success of the optimization process. As previously mentioned, the focus in this case has to be posed on the computed and measured trends of the performances of the parent and final hulls.

The procedure illustrated in Section 3.1 can use any simulated variable to monitor the quality of the solution. On the contrary, the V&V approach for CFD-based optimization has to be specifically applied to the objective function. Let us define $\mathscr{S}_{\mathscr{P}}$ and $\mathscr{S}_{\mathscr{O}}$ as the numerical simulation value of the parent and the optimized designs, respectively and define the corresponding numerical uncertainty as $U_{\mathscr{S}\mathscr{P}}$ and $U_{\mathscr{S}\mathscr{O}}$ (see Fig. 5). We also introduce $\mathscr{D}_{\mathscr{P}}$ as the experimental data for the parent hull and $\mathscr{D}_{\mathscr{O}}$ as the data for the optimized design, both with an associated experimental uncertainty $U_{\mathscr{D}\mathscr{P}}$ and $U_{\mathscr{D}\mathscr{O}}$. We also define

$$\Delta_{\mathscr{S}} = \mathscr{S}_{\mathscr{P}} - \mathscr{S}_{\mathscr{O}}, \tag{13a}$$

$$\Delta_{\mathscr{D}} = \mathscr{D}_{\mathscr{P}} - \mathscr{D}_{\mathscr{O}} \tag{13b}$$

as the expected ($\Delta_{\mathscr{S}}$) and the measured ($\Delta_{\mathscr{D}}$) differences between the two hulls. Obviously, if the problem is one of minimization of some objective function, $\Delta_{\mathscr{S}} > 0$ and $\Delta_{\mathscr{D}} > 0$ imply improvements of the final shape with respect to the parent hull.

To estimate the simulation error of the optimization process, $\delta_{\Delta\mathscr{S}}$, we can build on the analysis presented in the previous paragraph, decomposing the simulation error

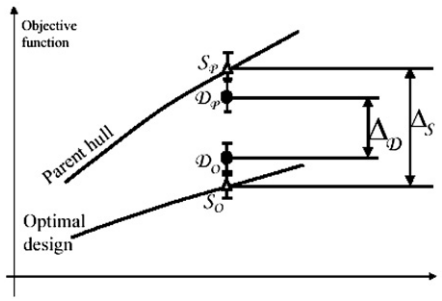

Fig. 5. Schematic representation of the set of data needed for the verification and validation approach for SBD. $\mathscr{S}_{\mathscr{P}}$ and $\mathscr{S}_{\mathscr{O}}$ are the numerical simulation values of the parent and the optimized designs. $\mathscr{D}_{\mathrm{P}}$ is the experimental data for the parent hull and $\mathscr{D}_{\mathscr{O}}$ as the data for the optimized design, both with an associated experimental uncertainty $U_{\mathscr{D}\mathscr{P}}$ and $U_{\mathscr{D}\mathscr{O}}$. Expected ($\Delta_{\mathscr{S}}$) and measured ($\Delta_{\mathscr{D}}$) differences between the two hulls are also shown.

into a numerical and a modeling component. Considering Eqs. (2) and (13a), we obtain:

$$\begin{aligned}\delta_{\Delta\mathscr{S}} &= (\delta^{\mathscr{P}}_{\mathscr{S}\mathscr{N}} + \delta^{\mathscr{P}}_{\mathscr{S}\mathscr{M}}) - (\delta^{\mathscr{O}}_{\mathscr{S}\mathscr{N}} + \delta^{\mathscr{O}}_{\mathscr{S}\mathscr{M}}) \\ &= (\delta^{\mathscr{P}}_{\mathscr{S}\mathscr{N}} - \delta^{\mathscr{O}}_{\mathscr{S}\mathscr{N}}) + (\delta^{\mathscr{P}}_{\mathscr{S}\mathscr{M}} - \delta^{\mathscr{O}}_{\mathscr{S}\mathscr{M}}), \qquad (14a)\\ \delta_{\Delta\mathscr{D}} &= (\delta^{\mathscr{P}}_{\mathscr{D}} - \delta^{\mathscr{O}}_{\mathscr{D}}). \qquad (14b)\end{aligned}$$

Assuming that the continuous equations used to model the problem remain valid for both the parent and the optimized hulls, it can be now reasonably argued that the modeling errors $\delta^{\mathscr{P}}_{\mathscr{S}\mathscr{M}}$ and $\delta^{\mathscr{O}}_{\mathscr{S}\mathscr{M}}$ are equal and that the last term of the RHS in (14a) is zero. In other terms, recalling the definition (3), we write

$$\delta^{\mathscr{P}}_{\mathscr{S}\mathscr{M}} - \delta^{\mathscr{O}}_{\mathscr{S}\mathscr{M}} = [\mathscr{M} - \mathscr{T}]_{\mathscr{P}} - [\mathscr{M} - \mathscr{T}]_{\mathscr{O}} = 0 \qquad (15)$$

and Eq. (14a) simplifies into the following:

$$\delta_{\Delta\mathscr{S}} = (\delta^{\mathscr{P}}_{\mathscr{S}\mathscr{N}} - \delta^{\mathscr{O}}_{\mathscr{S}\mathscr{N}}). \qquad (16)$$

Verification of the trend: With reference to the uncertainties, we now need a condition which states that if the expected improvement $\Delta_{\mathscr{S}}$ is greater than the simulation *numerical* noise $U_{\Delta\mathscr{S}}$ (according to (15) the simulation *modeling* errors for the parent and the optimal hull cancel each other), then the optimized design is numerically verified. From the error Eq. (16) hence follows the condition:

$$\begin{aligned}|\Delta_{\mathscr{S}}| > U_{\Delta\mathscr{S}} &= (U^2_{\mathscr{S}\mathscr{P}} + U^2_{\mathscr{S}\mathscr{O}})^{1/2} \\ &= (U^2_{\mathscr{S}\mathscr{N}\mathscr{P}} + U^2_{\mathscr{S}\mathscr{N}\mathscr{O}})^{1/2}. \qquad (17)\end{aligned}$$

Validation of the trend: In a similar manner, if the improvement measured in the experiment, $\Delta_{\mathscr{D}}$, is greater than the experimental noise, then the optimized design is experimentally verified.

$$|\Delta_{\mathscr{D}}| > (U^2_{\mathscr{D}\mathscr{P}} + U^2_{\mathscr{D}\mathscr{O}})^{1/2} = U_{\Delta\mathscr{D}}. \qquad (18)$$

Optimizer's validation: The definition (8) of the comparison error $\mathscr{E}$ has now to be modified into an *optimizer* error, $\mathscr{E}_{\Delta}$, focused on the trend. Hence, $\mathscr{E}_{\Delta}$ can be defined as the difference between the measured and the expected improvements, $\Delta_{\mathscr{D}}$ and $\Delta_{\mathscr{S}}$:

$$\mathscr{E}_{\Delta} = \Delta_{\mathscr{D}} - \Delta_{\mathscr{S}}. \qquad (19)$$

From (17) and (18), the corresponding uncertainty equation is

$$U_{\mathscr{E}_{\Delta}} = (U^2_{\Delta\mathscr{D}} + U^{\mathscr{P}2}_{\mathscr{S}\mathscr{N}} + U^{\mathscr{O}2}_{\mathscr{S}\mathscr{N}})^{1/2}. \qquad (20)$$

The last step is to state that if the difference between the measured and the expected improvements is less than the uncertainty $U_{\mathscr{E}_{\Delta}}$, that is

$$|\mathscr{E}_{\Delta}| \leqslant U_{\mathscr{E}_{\Delta}}. \qquad (21)$$

We may finally say that the optimized solution is validated at the interval $U_{\mathscr{E}_{\Delta}}$. It is worthwhile to observe that, as a consequence of (15), the condition (21) is stronger than the corresponding (12) because of the cancellation of the modeling errors in the optimization process. In other terms, the optimizer can be validated with a significant reduction in the interval of uncertainty.

4. The definition of the optimization problem

For the complete definition of the design problem to be solved, the following fundamental items must be precisely specified: (1) selection of an initial design to be optimized and of the extension of the modifiable region(s); (2) choice of the objective function to be minimized plus number and position of the design variables; and (3) definition of the problem's constraints. These steps are described in this paragraph.

4.1. Initial design

The initial design is Model 5415, which was conceived as a preliminary design for a US Navy surface combatant. The hull geometry includes both a sonar dome and transom stern, propulsion is provided through twin open-water propellers driven by shafts supported by struts. There is a large experimental database for Model 5415 due to an international collaborative study on experimental/numerical uncertainty assessment between IIHR, INSEAN and the Naval Surface Warfare Center, Carderock Division (NSWC), see Stern et al. [32]. The validation data includes global and local measurements, such as total resistance, boundary layer and wake, longitudinal wave cuts, bow and transom wave fields, and wave breaking. Two different views of the initial design are reported in Figs. 7 and 8 in comparison with the final, optimized shapes.

4.2. Objective function and design variables

The objective function f to be minimized is the total resistance R_{T} of the model 5415 advancing in calm water at a speed of $Fr = 0.28$. This condition corresponds to $Re = 1.67 \times 10^7$ when using a reference length of 5.72 m, that is the length of the ship's model used in the experimental validation (see last paragraph).

The modifiable region is only the foremost part of the ship, i.e., bow and the sonar dome (see Fig. 7), about 20% of the overall ship surface. As explained in the

introduction, this is the typical redesign problem of some part of an existing complex system, a necessity which often arises in real industrial applications. The test is a difficult one, because the optimizer has a reduced freedom and hence expected improvements are small. Also, the problem is solved for the bare hull. The geometrical complexity is hence partially reduced (e.g., no rudder and propeller will be considered here) but it must be underlined that in the bow redesign problem, both propeller and stern appendages show negligible influence.

A different number of design variables have been adopted in the two SBD frameworks. Indeed, number and location of the variables are closely connected with the specific strategies adopted to modify the ship's geometry and the computational meshes. For SBD-A, the displacements of the NURBS control points in the CAD-Based approach are the design variables of the optimization problem. Design actions of widely used CAD tools are emulated, so that control points defining the bow and sonar dome are moved in confined direction. That is, control points for the bow move only along the transverse direction (design variable d_{bt}). Those for the sonar dome move in transverse and longitudinal directions with d_{st} and d_{sl}, respectively. Control points are adequately grouped in order to avoid unrealistic shape modification (the bow and sonar dome groups include 15×14 and 15×7 points, respectively) and all the points in a group move with equal displacement in the same direction. For SBD-B, the variables are the control points of the patches used in the CAD-free approach. More precisely, 11 variables have been used for the parameterization of the deformation: with reference to Fig. 6, two variables serve for y-modifications of the region above the dome, four for the y-modification of the dome, three for the x-modification of the dome and two for the z-modification of the keel line below the dome.

4.3. Functional and geometrical constraints

To introduce elements of a real, complex design problem, functional and geometrical constraints have been enforced.

The functional constraints here adopted are relative to seakeeping and propulsion. In naval hydrodynamics, seakeeping characteristics give a measure of the behavior of the ship at sea: in this problem, the monitored quantities

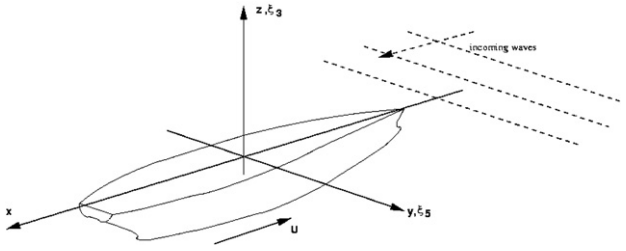

Fig. 6. Sketch of the problem. The ship is advancing with forward speed U in head sea.

are the peaks of the heave and pitch Response Amplitude Operator (RAO) curve for head seas (the RAO is the square of the amplitude of the regular wave transfer function at each frequency). Also, since sonar dome vortices quite often interfere with the propeller inflow affecting its performances, a functional constraint was put on the sonar dome vorticity as a source of non-uniformity of the flow at the propeller disk.

Geometrical constraints are imposed on the design variables, on the sonar dome volume, on the bow entry angle, on the displacement and on the principal dimensions of the ship. A complete definition of the problem, objective function and constraints, is given in Table 1.

5. Numerical results: the optimized designs

In the following we report the numerical solutions of the optimization problem defined before using the two SBD environments described in this paper. Indeed, being the SBDs assembled with different components (optimizers, numerical solvers, design tools) it is important to underline here that two different final shapes were expected. However, we anticipate that an analysis of the major characteristics of the two shapes will show that the final solutions display common geometrical trends. Hereinafter, the two final designs will be indicated as 5415-A (obtained using the SBD-A) and 5415-B (the SBD-B optimized shape).

While in the experiments the models are typically free to dynamically adjust their equilibrium under the action of the dynamic pressure field, the optimization process was carried out with the model in fixed condition: SBD-B assumed the model to be fixed at even keel, while SBD-A adopted the sinkage (σ) and trim (τ) values (shift and rotation around z and y axis, respectively, see Fig. 6) measured for the original 5415 model at $Fr = 0.28$. A free-model simulation was finally performed with SBD-B, to check the sensitivity to the exact sinkage and trim values. Results will be discussed later.

After some indications about the amount of computational work required in the solution of the design problem, the geometry and performances of the two improved shapes are described in comparison with those of the original design.

5.1. Numerical parameters and computational effort

The computational meshes used during the process were relatively coarse (of the order of 250 K grid points), even if they proved to be successful in guiding the optimization algorithms. However, the final shape was re-computed with a much finer grid (of the order of 1.75 M grid points) to check the estimated improvements.

SBD-A: The GA parameters adopted in the SBD-A optimizer for this test case are as follows: crossover rate = 0.75, mutation rate = 0.30, and population size = 60. As described earlier, the population size coincides with number of available parallel processors. The crossover

and mutation rates are determined through preliminary numerical tests. The optimal system parameters may be found by further investigation, but that is left for future work. In the present study, the best solution in 50 generations is selected as a final solution (i.e., model 5415-A), in which the solution was, in fact, obtained at the 21st generation. For each generation, RANS code is executed only once per processor, where 5000 global sweep iterations appeared to yield sufficient convergence. CPU time to proceed 10 generations is about 4 days by using PC-Cluster parallel computing environment mentioned earlier. Advantage of the present high performance parallel architecture is evident, since the CPU time would be 60 times larger if the conventional serial computation is adopted.

SBD-B: The computational domain extends 1.0 L_{PP} forward, 1.0 L_{PP} backward and 1.25 L_{PP} aside. A numerical beach is placed at the end of the grid, in order to damp out the outgoing waves. The grids are block-structured with hexahedrical elements, and the transom region has been properly modeled with a dedicated block. On the faces common to two blocks the cell distribution is unique.

The SBD-B used the variable-fidelity approach described before and only 36 calls to the high-fidelity solver (i.e., the finest grid) were required, while 314 calls to the low fidelity solver (the coarsest grid) were used. The CPU times for function evaluation with the low and high fidelity solvers are about 900 s and 5400 s, respectively. As a consequence, the complete optimization time with SBD-B has been roughly about 477,000 s (the time spent in grid and geometry manipulation is almost negligible). On the other hand, only 304 objective function values would have been necessary (after some saving) by using the high-fidelity model alone, with a total CPU time of 1,641,600 s. The final CPU time hence is only 29% of the total time needed by the high-fidelity procedure alone.

5.2. Optimized shapes and geometrical constraints

The optimization processes ended with two different geometries (Figs. 7–9) that however display some geometrical similarities as for the general trend. Indeed, a careful analysis of their shapes shows:

- a reduction of the maximum width of the dome (and of the dome volume), decreased by about 20% in the 5415-A case and by about 40% in the 5415-B shape;
- an increase of the length of the dome: the 5415-A sonar dome extension in the forward (x) direction (see Fig. 13) is about 10% of the total length of the dome itself. The trend toward a forward extension is observed also for the 5415-B, even if, due to the adopted grid topology which do not allows large variations on the bulb length in this region, the forward extension is only 1%;
- looking at the region immediately above the sonar dome, the reduction of the entry angle and the bending of the buttocks (hull contours at equal y). Differences

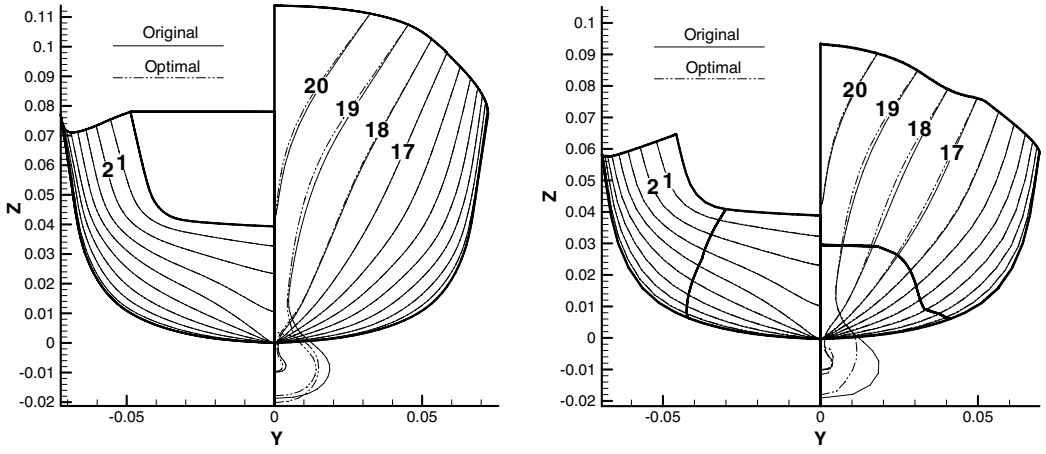

Fig. 7. Comparison of body plan between the original and optimal hull forms. Original 5415 vs. 5415-A (left) and original 5415 vs. 5415-B (right). Some transversal sections are numbered according to the conventional way to represent hull's geometry in ship hydrodynamics: the hull is divided into 20 sections, starting from the most aft (stern) station. Modifications were allowed from the foremost section (stem) down to Section 16.

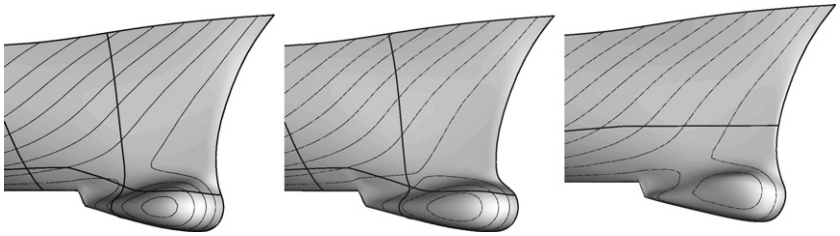

Fig. 8. Perspective view of the bow and sonar dome geometry. Original 5415 (left), 5415-A (center) and 5415-B (right).

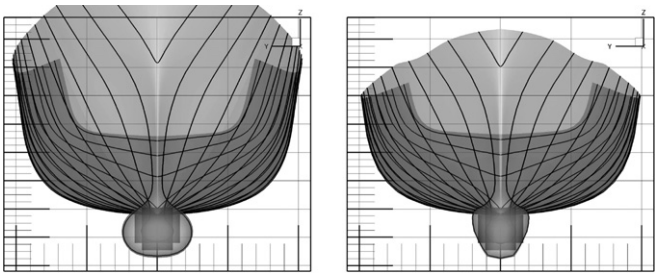

Fig. 9. The constraint on the sonar dome is verified both the optimized models 5415-A (left) and 5415-B (right). The two overlapping cylinders inside the dome represents the sonar arrays.

extend from the stem down to station 16 for model 5415-B, while for model 5415-A they remain confined between the extreme bow and station 18 (Fig. 7).

As a general comment, the volume reduction for the model 5415-A is rather uniform along the dome axis and the overall shape of the new dome is similar to the original (but for width and length). The 5415-B dome is slightly less conventional than the other two designs: the overall shape is more triangular (see Figs. 7 and 9) and in some points the hull surface is very close to the sonar constraint (Fig. 9), leading to a greater volume reduction.

Fig. 9 clearly shows that in both cases the constraint on the dome dimension is satisfied and the sonar fit inside the bulb. A close-up view of model 5415-B seems to display a slight violation of this constraint near the bottom corner. A careful analysis demonstrated that the minor violation is located in between two grid points and it is difficult to check geometrical details whose dimension is below the grid resolution. At all events, the minor violation is extremely small, being of the order of half of the grid cells near the body. The other geometrical constraints (entry angle and major dimension) have been successfully satisfied, as well as the displacement constraint, verified during the experimental campaign (see Section 6.2).

6. Performances analysis

In this paragraph we check the functional constraints and analyze the performances of the two new designs[2] as predicted by the simulations, in comparison with those of the parent hull 5415. Results from an experimental campaign are also illustrated here, while data relative to the V&V analysis applied to the two SBDs will be presented in the next chapter. It has to be remembered that the optimization was carried out with the hull fixed. An estimation of the effects of the ship's sinkage and trim is however given in the following.

[2] Influence of the particular solver on the final solution was not evaluated because, due to the different requirements in terms of grid topology, an exchange of the grid between the two solvers was impossible.

6.1. Performances and functional constraints prediction

The numerical results for the objective function, summarized in Table 2a (for the SBD-A) and b (for the SBD-B), show that both the SBDs were able to identify improved designs with lower total resistance with respect to the parent hull 5415.

The 5415-A model (Table 2a) displays a decrease of the objective function of −5.32% (from 45.40 N to 42.98 N). The optimization was performed with the model fixed at the sinkage and trim values measured at $Fr = 0.28$ ($\sigma = 8.29$ mm, $\tau = 0.05°$). A different way was followed with the SBD-B (Table 2b). The optimization was performed with the hull fixed at even keel ($\sigma = \tau = 0$) and, once the final shape (5415-B) was obtained it was let free to sink and trim, assuming a final value of $\sigma = 10.06$ mm, $\tau = 0.09°$ which correspond to a total resistance of 44.89 N. This value has to be compared with the 5415 total resistance 46.28 N at the sinkage and trim values measured at $Fr = 0.28$ ($\sigma = 8.29$ mm, $\tau = 0.05°$), giving a final reduction of the objective function of −3.01%.

Improved resistance reflects on the computed wave pattern too, as reported in Figs. 10 and 11. The wave field caused by the optimized hulls is globally smoother and with a smaller bow wave, a clear sign that the wave component of the ship's resistance has been reduced. A typical quantity to be monitored in these analyses is the wave profile along the hull (Fig. 12). Both the optimized models remarkably reduce the amplitude of the bow wave, 5415-A more then 5415-B. Furthermore, the steepness of the first wave and the first throat trough around model 5415-B are also appreciably smoothed. Fig. 13 shows improvements in the pressure coefficient distribution, with reduced low-values regions. The pressure pattern on the bow varies more gently and pressure gradients are reduced in the modified region.

Seakeeping computation have been performed to verify the corresponding functional constraints and the relative RAOs in head seas are showed in Fig. 14, while in Table 3 the threshold values of the constraints are reported.

Table 2
Optimization results for the objective function R_t

	R_t (N)	σ (mm)	τ (deg)
(a) SBD-A			
5415	45.40	8.29	0.05
5415-A	42.98	8.29	0.05
(b) SBD-B			
5415	46.28	8.29	0.05
5415	43.92	0.00	0.00
5415-B	41.84	0.00	0.00
5415-B	44.89	10.06	0.09

Both the SBD frameworks performed the optimization with the model in fixed condition. SBD-A assumed the sinkage and trim of the 5415 at $Fr = 0.28$ as fixed. SBD-B put the 5415 model at even keel and, after the optimization, moved the new model 5415-B to free sinkage and trim condition. Relative R_t reductions are –5.32% and –3.01% for SBD-A and SBD-B, respectively.

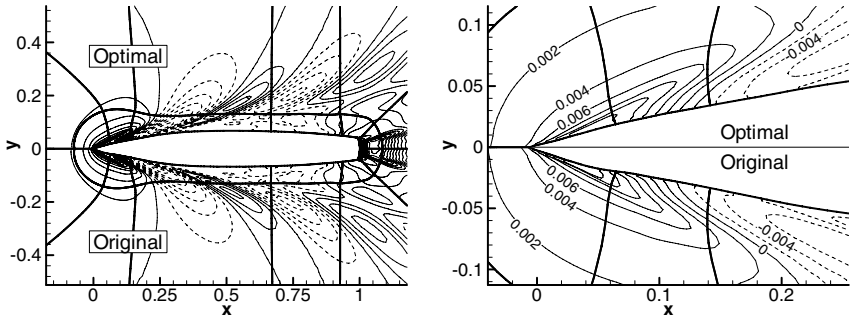

Fig. 10. Wave contours (non-dimensionalised by the model length) computed with the RANS free surface solver CFDSHIP-Iowa, adopted in SBD-A, around the original (bottom) and optimal (5415-A, top) ship model. Solid and dashed lines indicate positive and negative free surface height, respectively. The overall wave field is on the left, while on the right a close-up view of the bow region is shown. The bow wave is reduced, as well as the depth of the first throat.

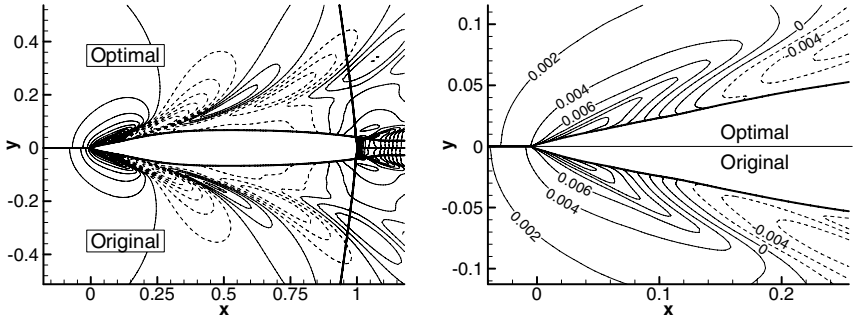

Fig. 11. Same as Fig. 10. The wave contours showed here (non-dimensionalised by the model length) are computed with the RANS free surface solver MGShip, adopted in SBD-B. The close-up view of the bow region shows that the maximum wave height is reduced, as well as the depth of the first throat.

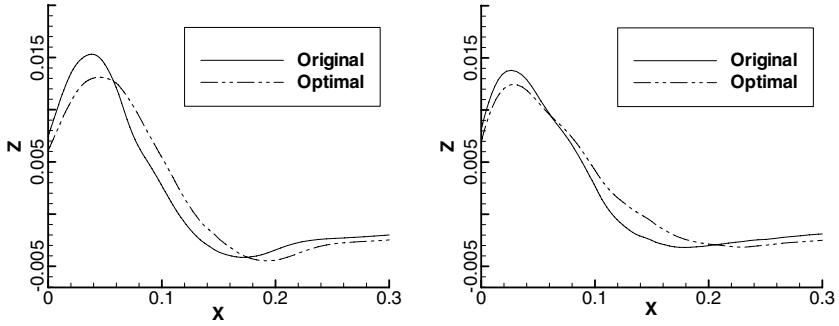

Fig. 12. Wave profiles along the hull in the bow region, as computed with CFDSHIP (left), and with MGShip (right) for the original and the two optimised shapes at the design speed. Both the RANS solvers predict a lower wave amplitude, a clear indication of a reduced wave component of the total resistance.

Model 5415-B show slightly improved seakeeping, more for the heave than for the pitch RAO, as a consequence of the change in the bow volume. Model 5415-A heave has been improved too, while the pitch response is substantially similar to that of the original hull. Hence, both the hulls respect the constraints on the vertical motions. Another functional constraint was imposed onto the problem (see Table 1), relative to the vorticity shed in the fluid by the dome. As stated before, this quantity is indirectly connected with the propulsion efficiency, since the sonar dome vortices typically travel along the side and the keel of the ship and finally interact with the flow seen by the propellers. The stronger are the vortices the less uniform is the propeller inflow. A control region was placed immediately past the sonar dome where the mean value of the axial vorticity should not overcome the average relative to the original hull. The axial vorticity contours reported in Fig. 15 clearly show that the constraint has been satisfied. The two final models reduce the core of the main vortex, which appears to be confined near the hull surface.

6.2. Experimental data for validation

To assess the success of the optimization process, obtaining basic data for the validation step, a dedicated experimental campaign was carried out. The campaign

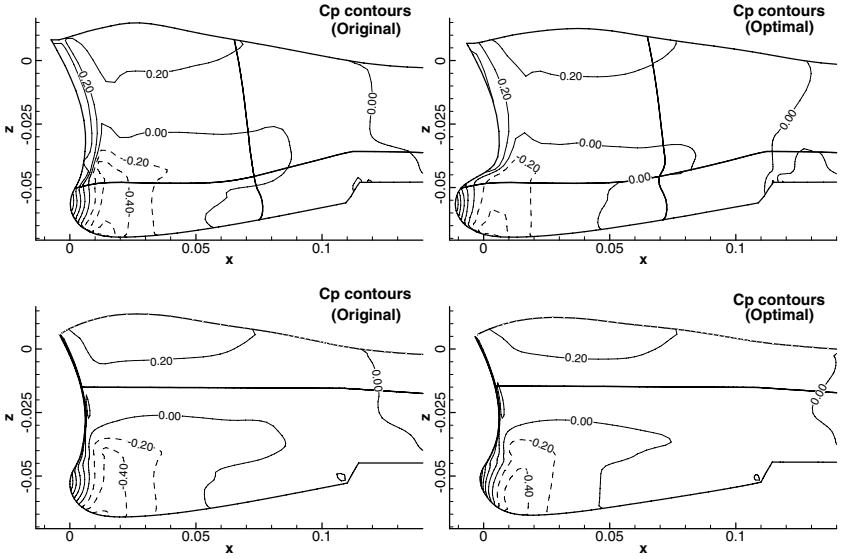

Fig. 13. Pressure coefficient (C_p) contours on the bow and the sonar dome of the original (left) and the optimal (right) ship model. Top, original 5415 vs. 5415-A, both computed with CFDSHIP-Iowa. Bottom, MGShip predictions for the original 5415 and the final solution 5415-B.

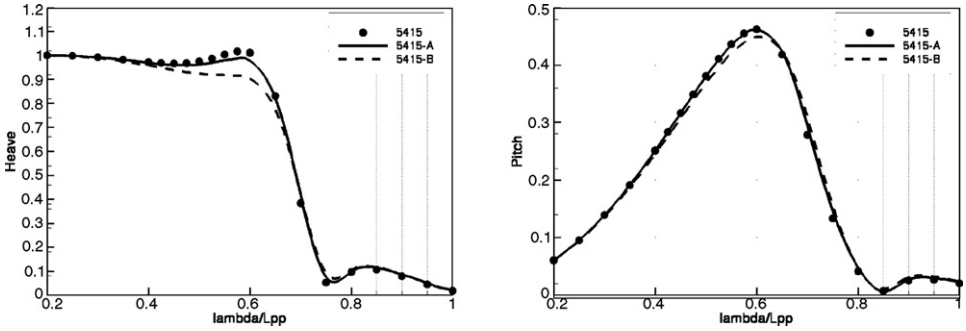

Fig. 14. The behavior of the ship in waves has been chosen as a functional inequality constraint. Heave (left) and pitch (right) frequency response (RAO) in head seas have been selected as performances to be monitored during the optimization process. Both the optimized models satisfy the requirements.

Table 3
Constraints on the seakeeping behavior of the two optimized ship (for the definitions see Table 1)

	5415	5415-A	5415-B	Constraint
H_C	1	0.983	0.981	1.020
P_C	1	0.996	0.970	1.020
S_C	1	0.989	0.975	1.000

used an existing replica of the DTMB 5415 (the INSEAN C.2340 model) already adopted in previous experiments [32]. Scale factor of the model was 24.824, giving a total length of 5.72 m a breadth of 0.771 m and a draft of 0.248 m. This values are compatible with the main dimensions of the INSEAN basin no. 2 (250 m long, 9 m wide and 4.5 m deep) and avoids blockage effects. All the resistance and seakeeping tests were carried out in this basin, equipped with a carriage capable of a maximum speed of 10 m/s with a precision on the forward velocity of about 0.1%. To further reduce the uncertainty connected to the model geometry, only the bow part of the new designs was build while the foremost part of original model was cut off and the model was prepared for the mounting of the two new bows (Fig. 16).

Displacement has to be measured for all the models, since the draught was fixed during the optimization process. It was found that the displacement of both the new hulls was reduced with respect to the original one in the limit posed by the constraint (max. 2%). Displacement for model 5415-A was 546.6 kg (8362 tons in ship scale, −0.44%), whereas for model 5415-B was 542.8 kg (8304 tons in ship scale, −1.13%) while for the original model was 549 kg (in ship scale, 8398 tons).

During the tests a load cell with a reading range of 200 N has been used. The same load cell has been applied for both the models and during the whole measurement campaign. Towing force has been registered during the experimental tests, together with the bow and stern sinkage. Uncertainty analysis was performed for two speeds: $Fr = 0.28$ (cruise speed and also design speed) and $Fr = 0.41$ (top speed), recording ten different resistance time histories. An admissibility test has been performed

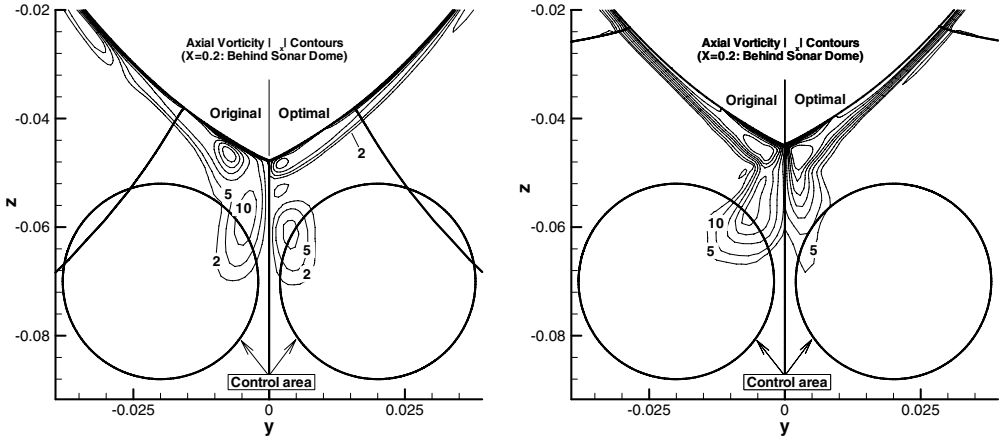

Fig. 15. Comparison of axial vorticity contours between the original and optimal hull forms ($X = 0.2$: behind sonar dome). The control region, placed in a plane orthogonal to the forward direction, is reported as a black circle. Original 5415 vs. 5415-A computed by CFDSHIP-Iowa (left), original 5415 vs. 5415-B computed with MGShip (right).

Fig. 16. Pictures for the experimental validation campaign. The original 5415 model (left) with the fore part cut off to host the optimized bows. In the center, the 5415-A bow mounted on the original body and ready for the tests. On the right, the bow of the 5415-B ready to be mounted.

on data, based on the variance of the whole dataset. Bias errors have been assumed from previous experiments [32].

The success of the optimization processes was confirmed by the experimental measurements. Reductions of the total resistance with respect to the original hull are directly reported in Fig. 17 as a function of the Froude number (values below 0% represent improved designs). At the design speed ($Fr = 0.28$) the measured reduction of the total resistance is about 3.80% for both the optimized models, while the uncertainties are clearly smaller than this

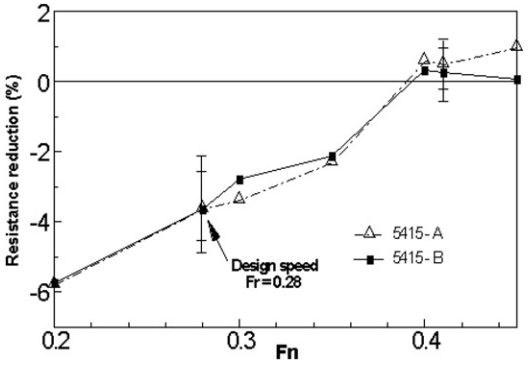

Fig. 17. Experimental validation of the numerical results. Resistance reduction (%) as a function of the Froude number for the two optimized models. Error bars are plotted for $Fr = 0.28$ and $Fr = 0.41$.

improvement. It may be of interest to look at off-design conditions too: in the whole tested speed range, the trend is similar for both the optimized models. A maximum reduction of about 6% is obtained at $Fr = 0.20$, while at the highest speed ($Fr = 0.41$) a very small increase is measured which however is well inside the error bar of the experimental uncertainty.

7. Verification and validation approach for SBD

The V&V analysis summarized in the following and reported in Tables 4 and 5 is based on the procedure illustrated in Sections 3.1 and 3.2. Initially, the numerical results are verified and validated as if they were single, isolated simulations (Table 4; U_{SPD} has been neglected in this paper). Finally, the two optimizers have been validated according to the new procedure developed in Section 3.2 (Table 5).

7.1. V&V for single numerical simulations

SBD-A: Grid convergence was studied by performing steady simulations using three computational grids with refinement $\sqrt{2}$ in each coordinate direction, i.e., of fine, medium, and coarse grids. The grid sizes of those grids are 1,779,648, 654,192, and 238,760, respectively. The

Table 4
V&V procedure for single numerical simulations relative to an integral quantity (the total resistance R_t)

RANS solver	Model	$\mathscr{S}$ (N)	$\mathscr{D}$ (N)	$\mathscr{E}$ (%)	$U_{\mathscr{D}}$ (%)	U_G (%)	U_{SN} (%)	U_V (%)
CFDSHIP-Iowa	5415	45.40	45.10	0.65	0.29	2.00	2.00	2.02
	5415-A	42.98	43.45	1.08	0.53	2.00	2.00	2.07
MGShip	5415	46.28	45.10	2.61	0.29	2.61	2.61	2.63
	5415-B	44.89	43.48	3.25	0.30	1.74	1.74	1.76

The quality of different RANS simulations on the parent hull and on the two optimized shapes is assessed separately following a V&V procedure [33]. Reported values of $\mathscr{D}$ refer to the total resistance R_t (N) scaled at a temperature of 15 °C.

Table 5
The modified V&V procedure for CFD-based optimization applied at the optimization results obtained with SBD-A and SBD-B ($\mathscr{P}$ = parent hull, $\mathscr{O}$ = optimized hull)

Optimization process	$\Delta_{\mathscr{S}} = \mathscr{S}_{\mathscr{P}} - \mathscr{S}_{\mathscr{O}}$	$\Delta_{\mathscr{D}} = \mathscr{D}_{\mathscr{P}} - \mathscr{D}_{\mathscr{O}}$	$U_{\Delta\mathscr{S}}$	$U_{\Delta\mathscr{D}}$	$\lvert\mathscr{E}_{\Delta}\rvert$	$U_{\mathscr{E}_{\Delta}}$
SBD-A	5.32	3.66	2.83	0.61	1.66	2.89
SBD-B	3.01	3.61	3.14	0.41	0.60	3.17

All values are in percentage. In both cases $|\mathscr{E}_{\Delta}| \leqslant U_{\mathscr{E}_{\Delta}}$ indicating that the optimized solutions are validated at the corresponding interval $U_{\mathscr{E}_{\Delta}}$.

predicted value of the 5415 total resistance value reported in Table 4 is $\mathscr{S} = 45,40$ N, very close to the experimental data, giving $|\mathscr{E}| = \mathscr{D} - \mathscr{S} = 0.65\%$, while for the 5415-A the estimated total resistance is lower than the experimental value, giving $|\mathscr{E}| = \mathscr{D} - \mathscr{S} = 1.08\%$.

Uncertainties in the data $U_{\mathscr{D}}$ are 0.29% for the original and almost doubled for the 5415-A (0.53%). Anyhow, in both cases the comparison error $\mathscr{E}$ is smaller than the validation uncertainty U_V%, hence the solution for total resistance is validated at the U_V interval.

SBD-B: Being MGShip a multigrid solver, a suite of refined grids is naturally available. Four grid sublevels were used with refinement ratio 2 in each coordinate direction and the three finest have been used in the V&V procedure. The predicted value of the total resistance of the parent hull is $\mathscr{S} = 46.28$ N (Table 4), with an error of about $|\mathscr{E}| = \mathscr{D} - \mathscr{S} = 2.61\%$. For the 5415-B the estimated total resistance is again greater than the experimental value, and the error is larger $|\mathscr{E}| = \mathscr{D} - \mathscr{S} = 3.25\%$.

Uncertainties in the 5415-B data U_D are almost equal to those of the 5415. Anyhow, in one case (for the original hull) the comparison error $\mathscr{E}$ is smaller than the validation uncertainty U_V%, and hence the solution is validated at the U_V interval. The solution is not validated at the U_V interval for the 5415-B model, likely due to a combination of factors: a larger error $\mathscr{E}$ and a smaller grid error which reduces U_V%.

7.2. V&V approach for CFD-based optimization

The V&V procedure for CFD-based optimization, illustrated before, is applied to the present optimization results to establish the success of the optimization.

The expected improvement $\Delta_{\mathscr{S}}$ estimated by SBD-A is 5.32% while the actual improvement $\Delta_{\mathscr{D}}$ is smaller. However, the error $\mathscr{E}_{\Delta}$ is smaller than the validation uncertainty $U_{\mathscr{E}_{\Delta}}$ and we finally may say that the optimized solution is validated at the interval $U_{\mathscr{E}_{\Delta}} = 2.89\%$. SBD-B predicts a smaller improvement $\Delta_{\mathscr{S}}$ of 3.01%, however very close to the actual improvement $\Delta_{\mathscr{D}}$. The error $\mathscr{E}_{\Delta}$ is smaller than the validation uncertainty $U_{\mathscr{E}_{\Delta}}$ and also the SBD-B optimized solution is validated at the interval $U_{\mathscr{E}_{\Delta}} = 3.17\%$.

8. Conclusions

Two different basic SBD versions have been developed and tested in a nonlinear constrained optimization problem. Experimental tests have been carried out on the two final optimized models, showing improvements in the objective function (the total resistance of the ship at model scale) while other important qualities of the ship, like the seakeeping behavior and the hydrodynamic noise produce by the sonar dome vortices, are preserved. This is a valuable results, considering the small modifications allowed and the good initial performances of the original model, and proves the applicability of RANS solvers inside an optimization cycle and the reliability design techniques based on simulations. Furthermore, the standard V&V procedure for CFD simulations has been extended to deal with CFD optimization results, focusing on the trend of the objective function. Its application to present results has validated both SBD approaches.

This application represents a first step into a cooperative project among IIHR, OPU and INSEAN which is extending toward multiobjective, global optimizations [6,38], hence removing the intrinsic limitations of local optimization algorithms. Indeed, typical feasible design spaces of nonlinear problems are non-convex and often non-connected, due to the nonlinear geometrical and functional constraints that have to be enforced to prevent unrealistic results and to provide a final, meaningful design. As a direct consequence, local optimizers may encounter convergence difficulties, besides the impossibility of jumping from one subset to another of the feasible set. Furthermore typical objective functions of hydrodynamic character display almost ever a multimodal nature, so that local optimizer are easily trapped in sub-optimal minima.

The adoption of global optimization algorithms may greatly reduce the risk of stopping the search at sub-optimal solutions. However, even if the use of RANS codes is facilitated by the availability of high performance computing platforms, the cost of one simulation is still relatively high. Under these circumstances the development of SBD frameworks which combine these costly analysis tools with global optimization algorithms may appear as a paradox, but design engineers of marine, aeronautical, automotive transport systems, are very much tempted by taking this direction [8].

Acknowledgements

The authors would like to thank Angelo Olivieri for the experimental data. Finally, EFC and DP thank Andrea Di Mascio for the use of RANS solver MGShip and Natalia Alexandrov for her continuous help.

References

[1] N.M. Alexandrov, A trust region framework for managing approximation models in engineering optimization, in: 6th AIAA/NASA/ISSMO Symp. on Multidisciplinary Analysis and Opt., AIAA-96-4102, 1996.
[2] N.M. Alexandrov, R.M. Lewis, C.R. Gumbert, L.L. Green, P.A. Newman, Optimization with variable-fidelity models applied to wing design, in: 38th Aerospace Sciences Meeting & Exhibit, Reno, USA, AIAA 2000-0841, 2000.
[3] N.M. Alexandrov, R.M. Lewis, First-order approximation and model management in optimization, in: L.T. Biegler, O. Ghattas, M. Heinkenschloss, B. van Bloemen Waanders (Eds.), Large-Scale PDE-Constrained Optimization, Lecture notes in Computational Science and Engineering, Springer, 2003.
[4] L.T. Biegler, O. Ghattas, M. Heinkenschloss, B. van Bloemen Waanders (Eds.), Large-Scale PDE-Constrained Optimization, Lecture notes in Computational Science and Engineering, Springer, 2003.
[5] C. Bischof, A. Carle, G. Corliss, A. Grienwank, P. Hovland, ADIFOR: generating derivative codes from Fortran programs, Sci. Programm. 1 (1) (1992) 11–29.
[6] E.F. Campana, D. Peri, A. Pinto, F. Stern, Y. Tahara, A comparison of global optimization methods with application to ship design, in: 5th Osaka Coll. on Advanced CFD Applications to Ship Flow and Hull Form Design, Osaka, Japan, 2005.
[7] K.J. Chang, R.T. Haftka, G.L. Giles, P.J. Kao, Sensitivity-based scaling for approximating structural response, J. Aircraft 30 (2) (1993) 283–288.
[8] S.E. Cox, R.T. Haftka, C.A. Baker, B. Grossman, W.H. Mason, L.T. Watson, A comparison of global optimization methods for the design of a high-speed civil transport, J. Global Optimiz. 21 (2001) 415–433.
[9] H.W. Coleman, F. Stern, Uncertainties in CFD code validation, ASME J. Fluids Engrg. 119 (1997) 795–803.
[10] L. Davis, Handbook of Genetic Algorithms, Van Nostrand Reinhold, A Division of Wadsworth, Inc., 1990.
[11] A. Di Mascio, R. Broglia, B. Favini, A second-order Godunov-type scheme for Naval Hydrodynamics, in: Godunov Methods: Theory and Application, Kluwer Academic Publishers, Singapore, 2000.
[12] R. Duvigneau, M. Visonneau, Hybrid genetic algorithms and artificial neural networks for complex design optimisation in CFD, Int. J. Numer. Methods Fluids 44 (2004) 1257–1278.
[13] R. Giering, T. Kaminski, Recipes for adjoint code construction, ACM Trans. Math. Software 24 (4) (1998) 437–474.
[14] Gothenburg, http://www.iihr.uiowa.edu/gothenburg2000, 2000.
[15] A. Griewank, Evaluating derivatives: Principles and Techniques of Algorithmic Differentiation, SIAM, Philadelphia, USA, 2000.
[16] R.T. Haftka, Combining global and local approximations, AIAA J. 29 (1991) 1523–1525.
[17] J. Holland, Adaptation in Natural and Artificial Systems, University of Michigan Press, Ann Arbor, USA, 1975.
[18] A. Jameson, Aerodynamic design via control theory, J. Sci. Comput. 3 (1988) 233–260.
[19] L. Larsson, F. Stern, V. Bertram, Benchmarking of computational fluid dynamics for ship flows: The Gothenburg 2000 Workshop, J. Ship Res. 47 (1) (2003) 63–81.
[20] W.G. Meyers, T.R. Applebee, A.E. Baitis, User's Manual for the Standard Ship Motion Program, SMP, Software Documentation, DTNSRDC/SPD-0936-01.
[21] B. Mohammadi, O. Pironneau, Applied Shape Optimization for Fluids, Clarendon Press, Oxford, UK, 2001.
[22] B. Mohammadi, O. Pironneau, Shape Optimization in Fluid Mechanics, Ann. Rev. Fluid Mech. 36 (2004) 255–279.
[23] J.N. Newman, Marine Hydrodynamics, The MIT Press, Cambridge, USA, 1977.
[24] J.C. Newman III, R. Pankajakshan, D.L. Whitfield, L.K. Taylor, Computational design optimization using RANS, in: 24th Symp. on Naval Hydro., Fukuoka, Japan, 2002.
[25] E.G. Paterson, R.V. Wilson, F. Stern, General-purpose parallel unsteady RANS ship hydrodynamics code: CFDSHIP-Iowa, The University of Iowa, IIHR Report No. 432, 2003.
[26] D. Peri, E.F. Campana, High fidelity models in the multi-disciplinary optimization of a frigate ship, in: 2nd MIT Conf. on Fluid and Solid Mech., Cambridge, USA, 2003.
[27] D. Peri, E.F. Campana, Multidisciplinary design optimization of a naval surface combatant, J. Ship Res. 41 (1) (2003) 1–12.
[28] D. Peri, E.F. Campana, High fidelity models in simulation based design, in: 8th Int. Conf. on Numerical Ship Hydro., Busan, South Korea, 2003.
[29] D. Peri, E.F. Campana, High-fidelity models and multiobjective global optimization algorithms in simulation based design, J. Ship Res. 49 (3) (2005) 159–175.
[30] O. Pironneau, Optimal Shape Design for Elliptic Systems, Springer-Verlag, New York, USA, 1984.
[31] P.R. Spalart, S.R. Allmaras, One-equation turbulence model for aerodynamic flows, La Recherche Aerospatiale 1 (1994) 5–21.
[32] F. Stern, J. Longo, R. Penna, A. Olivieri, T. Ratcliffe, H.W. Coleman, International collaboration on benchmark CFD validation data for surface combatant DTMB model 5415, in: 23rd Symp. on Naval Hydro., Val de Ruil, France, 2000.
[33] F. Stern, R.V. Wilson, H.W. Coleman, E.G. Paterson, Comprehensive approach to verification and validation of CFD simulations—Part 1: Methodology and procedures, J. Fluids Engrg. 123 (2001) 793–802.
[34] F. Stern, R.V. Wilson, J. Longo, P. Carrica, T. Xing, T. Tahara, C. Simonsen, J. Kim, J. Shao, M. Irvine, M. Kandysamy, S. Gosh, G. Weymouth, Paradigm for development of simulation based design for ship hydrodynamics, in: 3rd Int. Conf.: Navy And Shipbuilding Nowadays (NSN'2003), Krylov Shipbuilding Research Institute, St. Petersburg, Russia, 2003.
[35] Y. Tahara, F. Stern, A large-domain approach for calculating ship boundary layers and wake for nonzero Froude number, J. Comput. Phys. 127 (2) (1996) 398–411.
[36] Y. Tahara, T. Katsui, M. Kawasaki, K. Kodama, Y. Himeno, Development of large-scale high-performance CFD coding method for PC-cluster Parallel Comp. Environment 1st Report: Setup and Initial Evaluation of Coding Environment with MPI Protocol, J. Kansai Soc. Naval Arch. (241) (2004).
[37] Y. Tahara, F. Stern, Y. Himeno, Computational fluid dynamics-based optimization of a surface combatant, J. Ship Res. 28 (4) (2004) 273–287.
[38] Y. Tahara, D. Peri, E.F. Campana, F. Stern, CFD-based multiobjective optimization of a surface combatant, in: 5th Osaka Coll. on Advanced CFD Applications, Osaka, Japan, 2005.
[39] M. Valorani, D. Peri, E.F. Campana, Sensitivity analysis methods to design optimal ship hulls, Optimiz. Engrg. 4 (2003) 337–364.
[40] R.V. Wilson, E. Paterson, F. Stern, Verification and validation for RANS simulation of a naval combatant, in: Workshop on Numerical Ship Hydro, Gothenburg, Sweden, 2000.
[41] R.V. Wilson, F. Stern, H.W. Coleman, E.G. Paterson, Comprehensive approach to verification and validation of CFD simulations—Part 2: Application for RANS simulation of a cargo/container ship, J. Fluids Engrg. 123 (2001) 803–810.
[42] R.V. Wilson, P. Carrica, H. Hyman, F. Stern, A steady and unsteady single-phase level set method for large amplitude ship motions and maneuvering, in: 25th Symp. on Naval Hydro., St John's, Canada, 2004.